Electronic Supplementary Information

for

Transformation of Tetranuclear [{MoO₃(Lᶜᵃᵗ)Cu}₂]²⁻ into Trinuclear [MoO₂(Lᶜᵃᵗ)₂Cu₂] and Possible Implications on the Formation of Bis(MPT)Mo by MobA

A. M. Buddhika Chandima,[a]‡ Umesh I. Kaluarachchige Don,[a]‡ Cassandra L. Ward,[b] Richard L. Lord,[*c] Stanislav Groysman[*a]

[a]Department of Chemistry, Wayne State University, 5101 Cass Ave. Detroit MI 48202.

[b]Lumigen Instrument Center, Wayne State University, 5101 Cass Avenue, Detroit, Michigan 48202, United States.

[c]Department of Chemistry, Grand Valley State University, 1 Campus Drive, Allendale, Michigan 49401

E-mails: groysman@wayne.edu, lordri@gvsu.edu

‡ These authors contributed equally to this work.

Table of Contents

1. General experimental details

All reactions involving air-sensitive materials were carried out in a nitrogen-filled glovebox. 2,7-Di-tert-butyl-9,9-dimethyl-4,5-diaminoxanthene, $L^{cat}H_2$ ligand (**Scheme S1**) and tetraethylammonium molybdate were synthesized using previously published procedures.[1-3] Tetrakis(acetonitrile)copper(I) hexafluorophosphate was purchased from Millipore-Sigma and used as received. All non-deuterated solvents were purchased from Millipore-Sigma and were of HPLC grade. The non-deuterated solvents were purified using an MBraun solvent purification system. Dichloromethane-d_2 and acetonitrile-d_3 were purchased from Cambridge Isotope Laboratories. All solvents were stored over 3 Å molecular sieves. Compounds were generally characterized by ^1H and ^{13}C NMR spectroscopy (including 2D techniques such as ^1H-^1H COSY and HMBC), high-resolution mass spectrometry, and X-ray crystallography. The characterization was carried out at the Lumigen Instrument Center at Wayne State University. NMR spectra were recorded on an Agilent DD2-600 MHz Spectrometer, a Varian VNMRS-500 MHz Spectrometer and an Agilent 400 MHz Spectrometer in CD_2Cl_2 at room temperature or CD_3CN at various temperatures (room temperature to 50 °C). Chemical shifts and coupling constants (J) were reported in parts per million (δ) and Hertz respectively. Detailed assignments of the signals in ^1H NMR are given in the ESI. High resolution mass spectra (unless otherwise stated) were collected on a Thermofisher Scientific LTQ Orbittrap XL mass spectrometer. The MS survey scan was set from 200 – 2000. The resolution was set to 60000. In all cases, only one microscan was used in the analysis. HRMS for ligand run using a LCT Premier XE with a range of 200 – 2000 scans. Leucine Enkephalin was used as a lockmass. UV-visible spectra were obtained on a Shimadzu UV-1800 spectrometer.

2. Synthesis of ligand L^catH_2.[3]
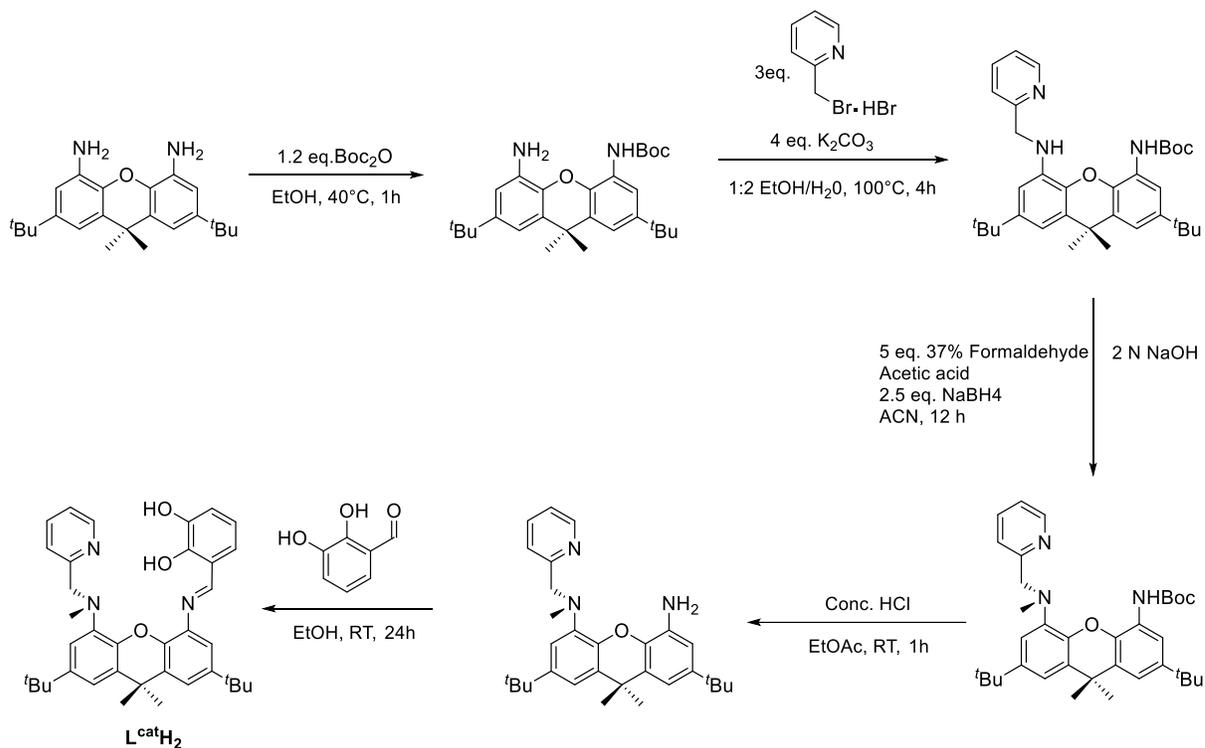
Scheme S1. Synthesis of L^catH_2.[3]

Synthesis of the heterodinucleating ligand (L^catH_2) was carried out as described in **Scheme S1**. The synthesis of the heterodinucleating ligand (L^catH_2) is initiated from xanthene diamine that is obtained in two steps from the commercially available xanthene dicarboxylic acid. The synthesis of L^catH_2 involved initial protection of one of the amine sites by tert-butyloxycarbonyl (BOC), followed by alkylation of the second position, methylation at the unprotected amine, deprotection and condensation reaction to obtain the final product L^catH_2 which was isolated in the overall yield of 38%. The full experimental and characterization details are provided elsewhere.[3]

3. Synthesis and Characterization of (NEt₄)₂[MoO₃(Lᶜᵃᵗ)] (1)

A 3 mL solution of tetraethylammonium molybdate $(NEt_4)_2[MoO_4]$ (15 mg, 0.036 mmol) in CH_3CN and a 3 mL solution of $L^{cat}H_2$ (20 mg, 0.036 mmol) in THF were prepared and cooled to -33 °C. The solution of cold $L^{cat}H_2$ was then added dropwise to a stirring solution of cold $(NEt_4)_2[MoO_4]$. The reaction mixture was stirred for 15 minutes, after which the volatiles were removed in vacuo to produce a lemon-yellow solid of $(NEt_4)_2[MoO_3(L^{cat})]$ (**1**) (31 mg, 0.032 mmol, 89%).

^1H NMR (400 MHz, CD₃CN) δ 8.89 (s, 1H), 8.39 (d, $J = 4.6$ Hz, 1H), 7.41 (td, $J = 8.0, 2.0$ Hz, 1H), 7.26 (d+s, $J = 2$ Hz, 2H), 7.05 (s+m, 3H), 6.92 (d, $J = 2.3$ Hz, 1H), 6.81 (d, $J = 2.3$ Hz, 1H), 6.34 (dd, $J = 8.0, 2.0$ Hz, 1H), 6.17 (t, $J = 7.7$ Hz, 1H), 4.60 (s, 2H), 3.15 (q, $J = 8.0$ Hz, 16H), 2.87 (s, 3H), 1.61 (s, 6H), 1.35 (s, 8H), 1.23 (s, 9H), 1.14 (t, $J = 8.0$ Hz, 24H).

^{13}C NMR (101 MHz, CD₃CN) δ 165.30, 161.78, 160.44, 160.27, 151.08, 149.65, 146.70, 145.85, 143.66, 142.38, 140.25, 137.36, 131.12, 131.05, 123.66, 122.66, 119.91, 118.83, 116.18, 115.80, 115.72, 114.22, 113.24, 112.85, 61.03, 53.03, 41.92, 35.74, 35.35, 35.28, 32.21, 31.89, 31.71, 7.74.

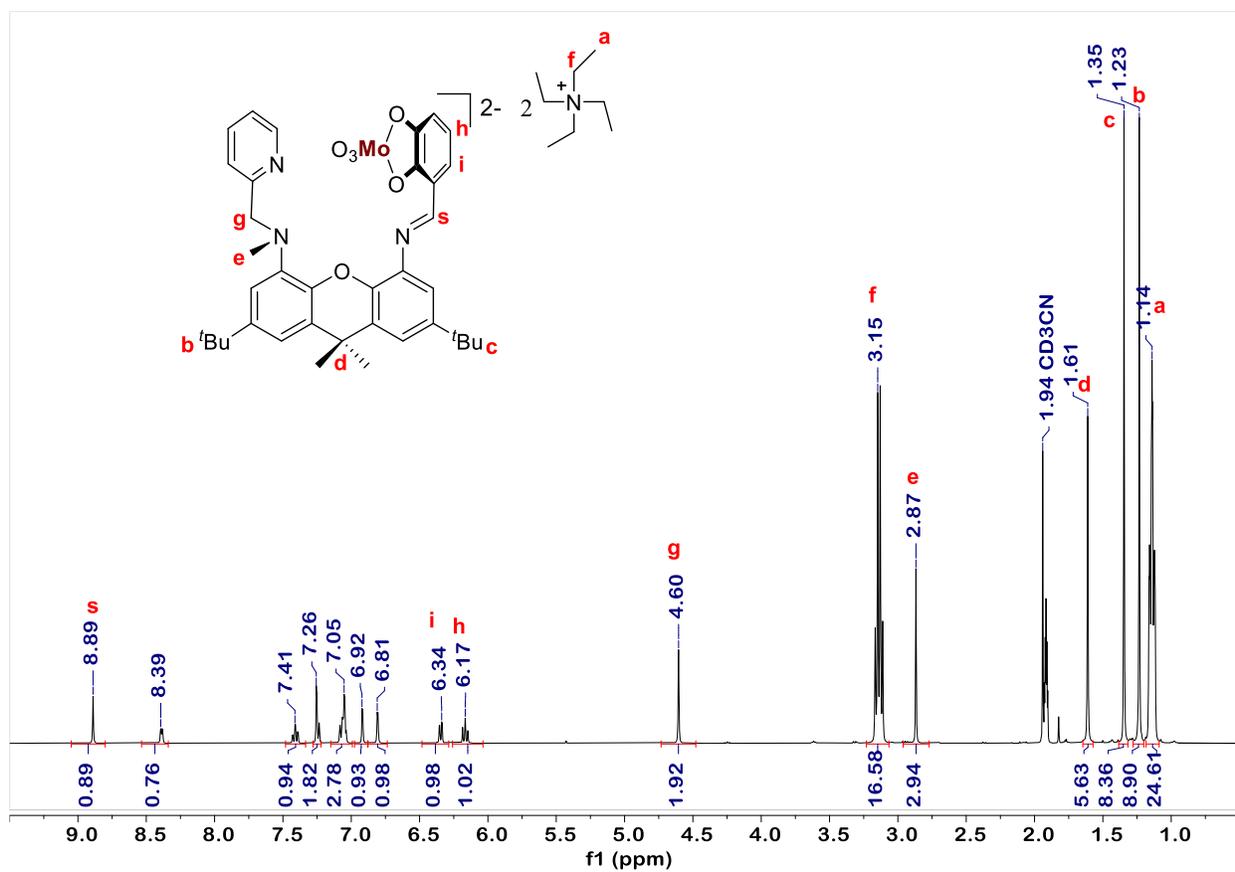HRMS (ESI⁺) m/z 722.2164 (calculated m/z for $\{[MoO_3(L^{cat})] + H\}^+$ 721.2128).

Figure S1. ^{1}H NMR spectrum of $(NEt_4)_2[MoO_3(L^{cat})]$ (CD_3CN, 400 MHz).
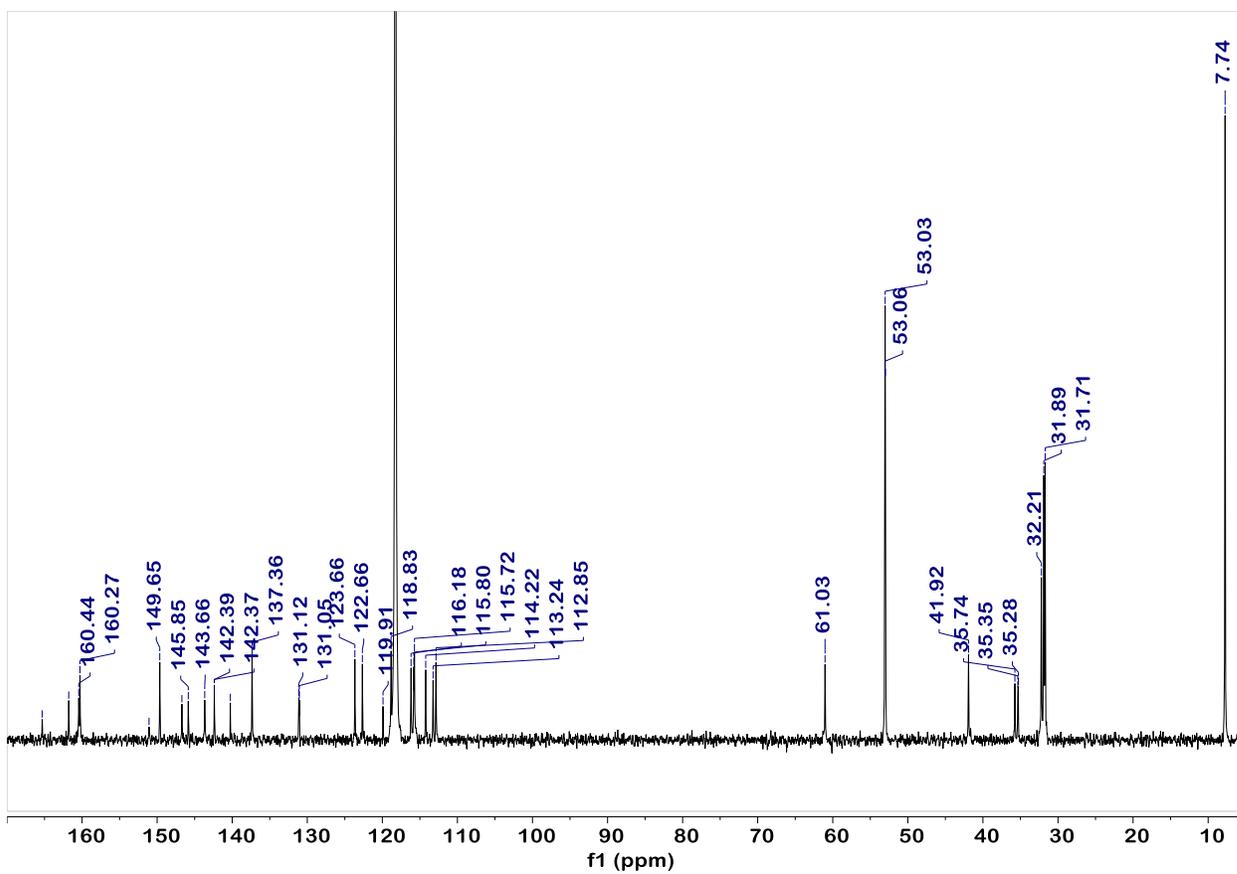
Figure S2. ^{13}C $\{^1H\}$ NMR spectrum of $(NEt_4)_2[MoO_3(L^{cat})]$ (CD$_3$CN, 600 MHz).
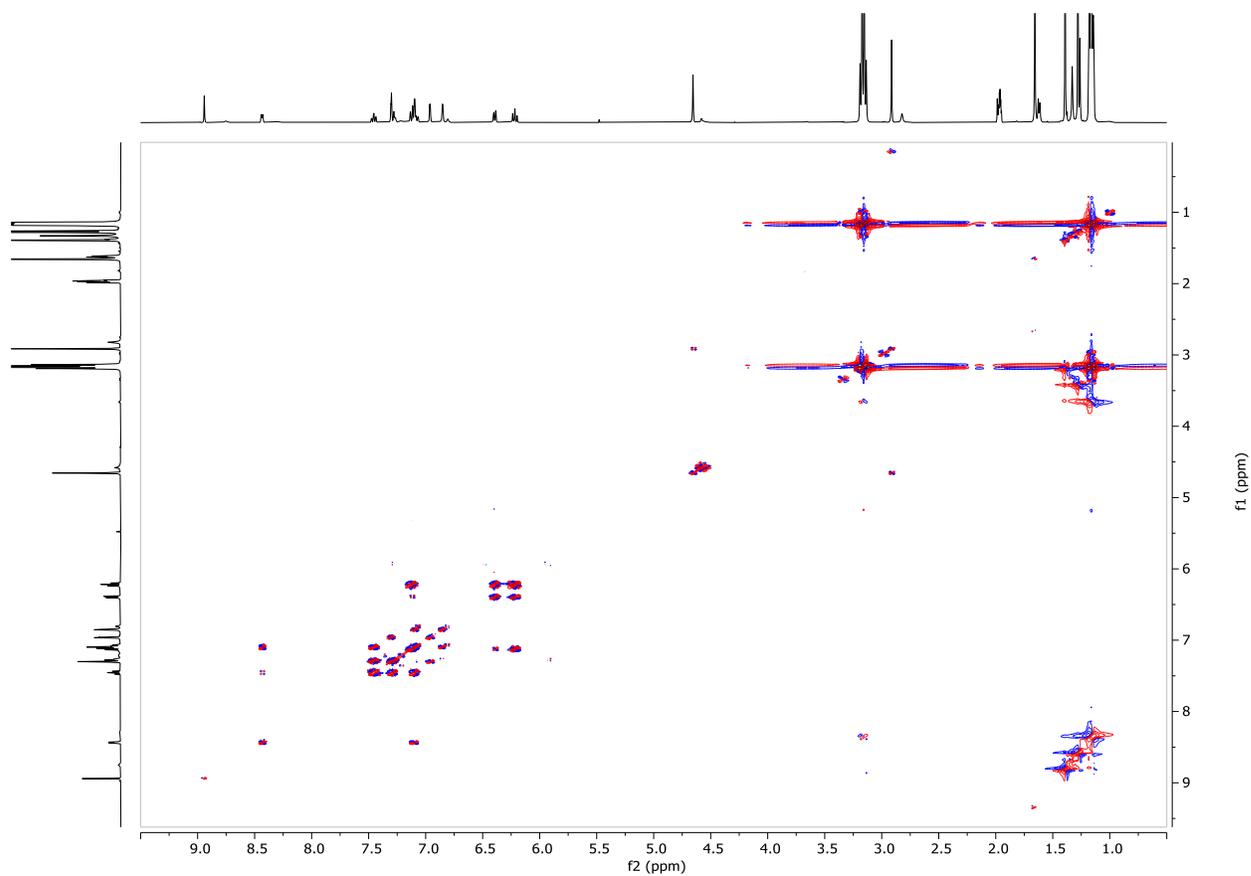
Figure S3. ^{1}H-^{1}H COSY NMR spectrum of (NEt$_4$)$_2$[MoO$_3$(L^{cat})] (CD$_2$Cl$_2$, 400 MHz).
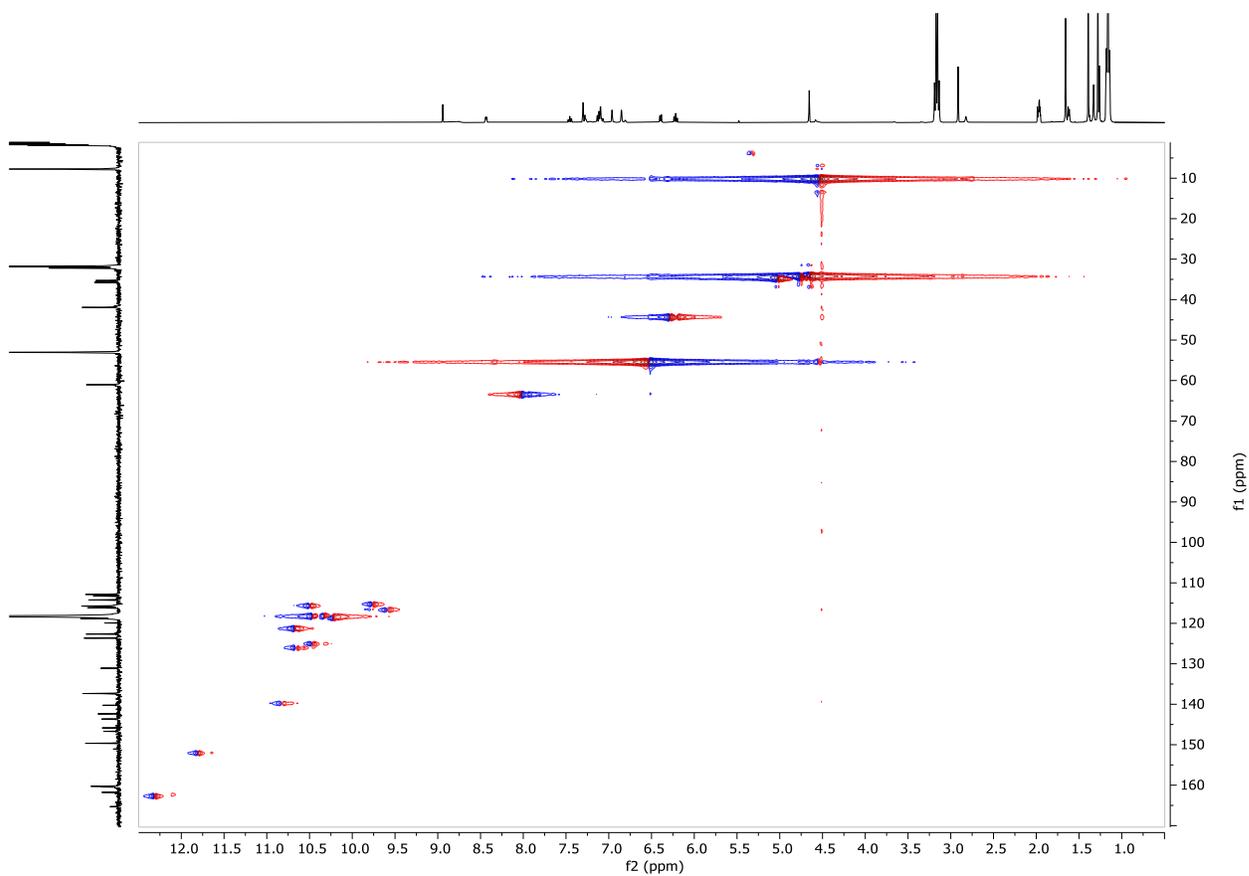
Figure S4. ^{1}H-^{13}C HSQC NMR spectrum of $(NEt_4)_2[MoO_3(L^{cat})]$ (CD_2Cl_2, 400 MHz).

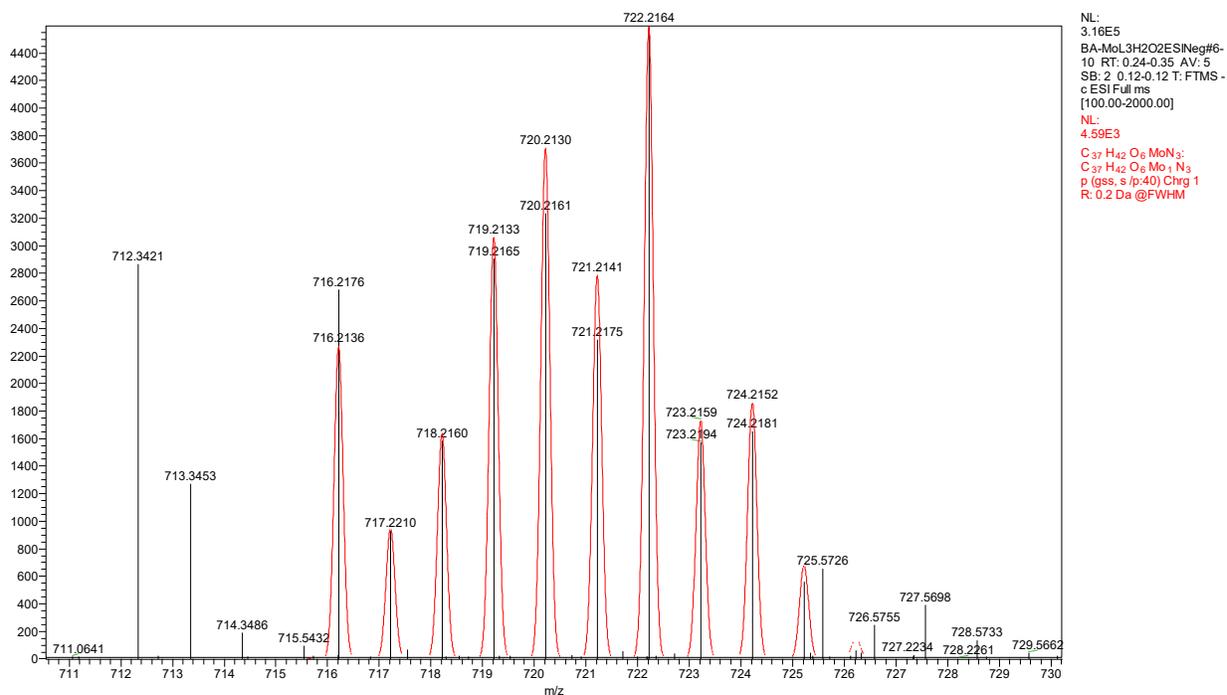**Figure S5.** High-resolution mass spectrum of $(NEt_4)_2[MoO_3(L^{cat})]$, demonstrating the peak attributed to [M+H]. The m/z peak at 722.2164 corresponds to the mass of the metal complex with one proton added $[M+H]^-$, expected value of 721.2128.

4. Synthesis and Characterization of (NEt$_4$)$_2$[{MoO$_3$(L^{cat})Cu}$_2$] (2)

A 3 mL solution of L^{cat}H$_2$ (26 mg, 0.045 mmol) in THF and a 3 mL solution of (NEt$_4$)$_2$[MoO$_4$] (19 mg, 0.045 mmol) in CH$_3$CN were prepared and cooled to -33 °C. The solution of cold L^{cat}H$_2$ was then added dropwise to a stirring solution of cold (NEt$_4$)$_2$[MoO$_4$]. The reaction mixture was stirred for 15 minutes and 3 ml solution of tetrakis(acetonitrile)copper(I) hexafluorophosphate [Cu(NCMe)$_4$](PF$_6$) (16.8 mg, 0.045 mmol, 1.0 equiv.) was added. The reaction mixture was stirred for 5 minutes, after which the volatiles were removed in vacuo to produce a dark orange solid and crude product was recrystallized using CH$_3$CN/ether at -33 °C to give dark orange crystals of **2** (34 mg, 0.016 mmol of **2**, 71%). The yield was calculated based on the chemical formula obtained from the crystal structure of **2** that includes co-crystallized solvents (see Table S1).

^{1}H NMR (400 MHz, CD$_3$CN) δ 8.48 (s, 1H), 8.05 (d, J = 8.0 Hz, 1H), 7.57 (t, J = 8.0 Hz, 1H), 7.39 (d, J = 8.0 Hz, 1H), 7.30 (s, 1H), 7.27 (s, 1H), 7.22 (s, 1H) 7.08 (s, 1H), 6.93 (t, J = 8.0 Hz, 1H), 6.68 (d, J = 8.0 Hz, 2H), 6.64 (d, J = 8.0 Hz, 2H), 6.43 (t, J = 8.0 Hz, 1H), 5.39 (s, 2H), 3.36 (s, 3H), 3.16 (q, J = 8.0 Hz, 12H), 1.59 (s, 6H), 1.36 (s, 9H), 1.23 (s + t, t-Bu + NCH$_2$CH$_3$, 21H).

^{13}C NMR (101 MHz, CD$_2$Cl$_2$) δ 164.19, 159.99, 151.64, 149.29, 146.71, 146.39, 146.24, 142.43, 142.34, 140.72,133.64, 135.49, 132.11, 130.68, 123.52, 123.41, 122.39, 121.78, 119.23, 119.13, 117.70, 117.02, 116.61, 116.41, 61.45, 42.54, 35.69, 35.33, 35.29, 32.37, 31.93, 31.90.

HRMS (ESI$^+$) m/z 785.1413 (calculated m/z for {MoO$_3$(L^{cat})Cu}$^+$ 785.1422.
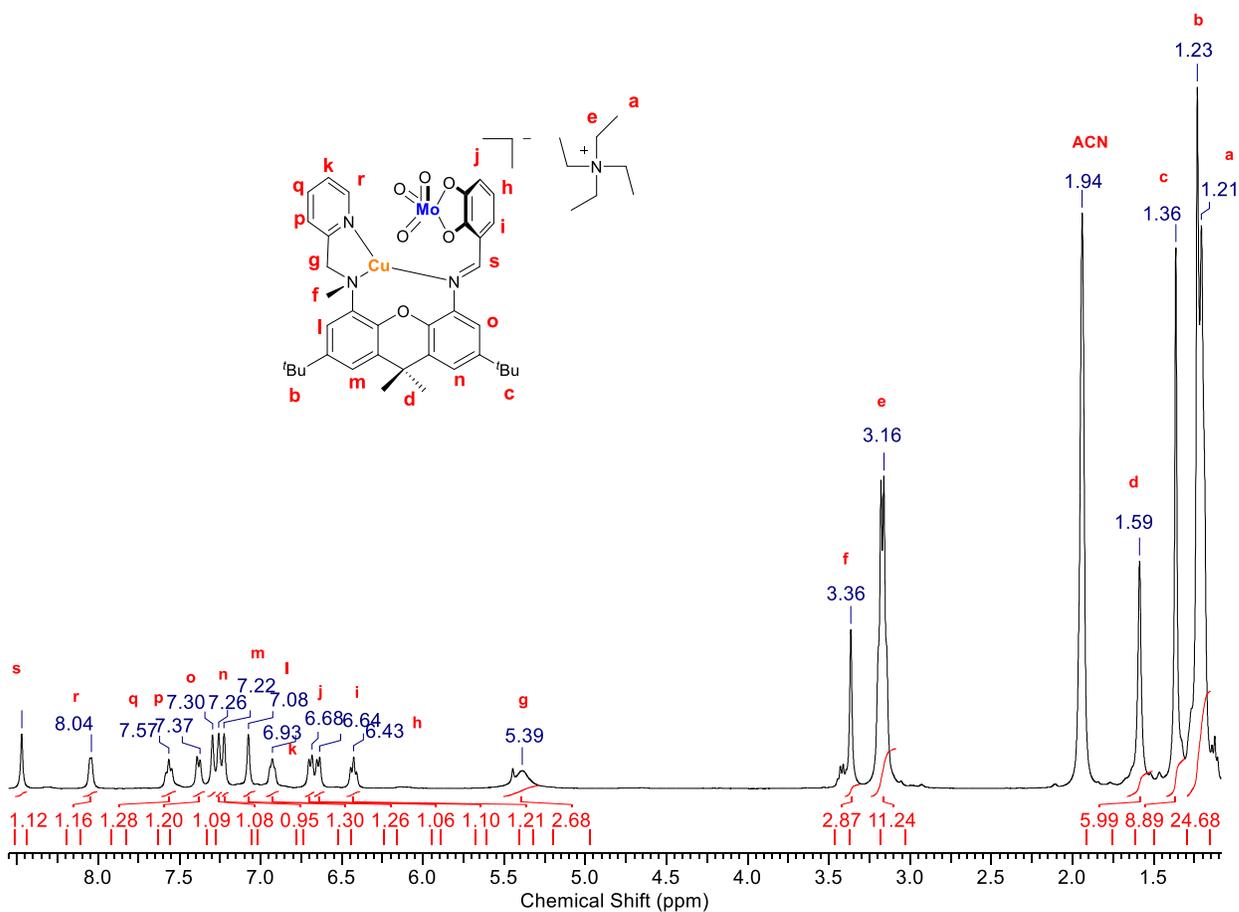
Figure S6. ^{1}H NMR spectrum of $(NEt_4)_2[\{MoO_3(L^{cat})Cu\}_2]$ (**2**) (CD$_3$CN, 400 MHz).
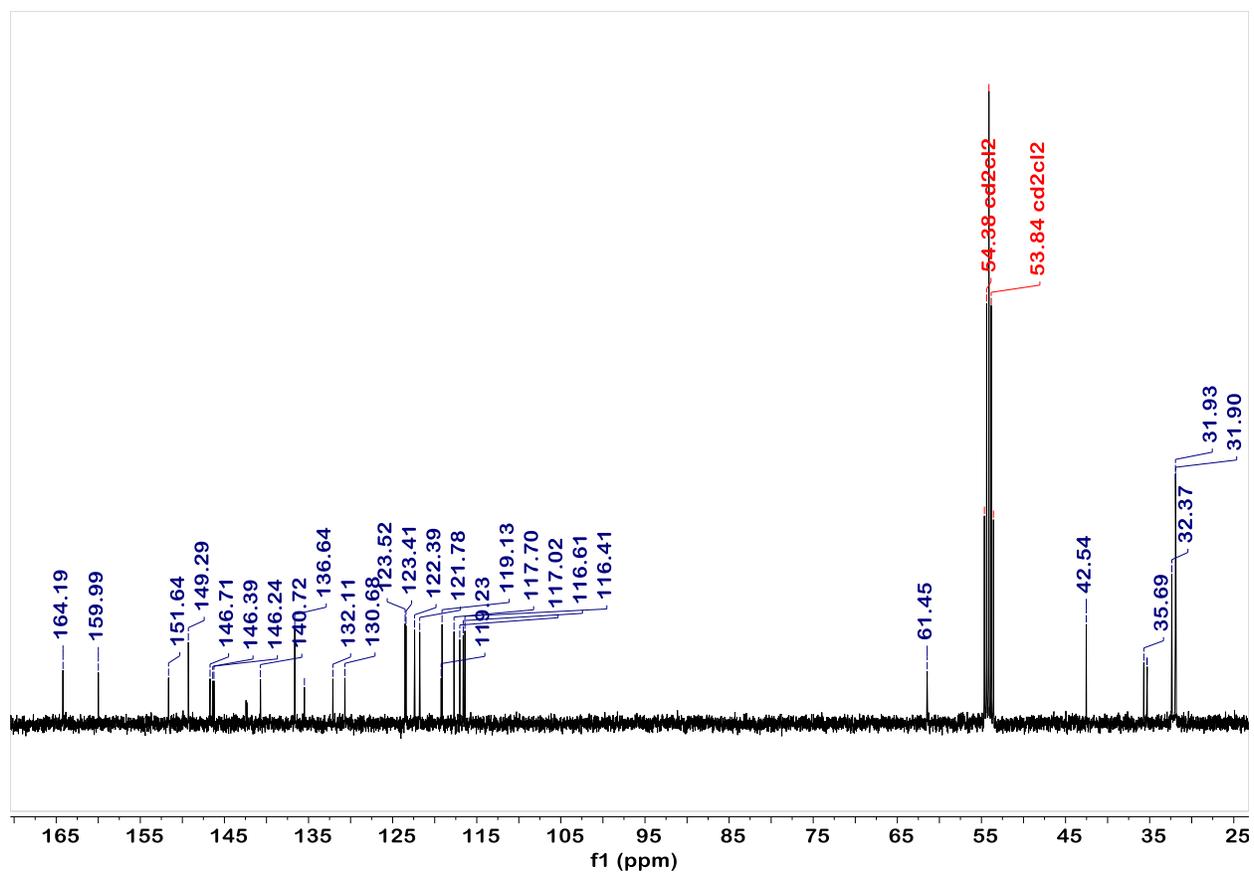
Figure S7. ^{13}C {^1H} NMR spectrum of $(NEt_4)_2[\{MoO_3(L^{cat})Cu\}_2]$ (**2**) (CD$_3$CN, 101 MHz).
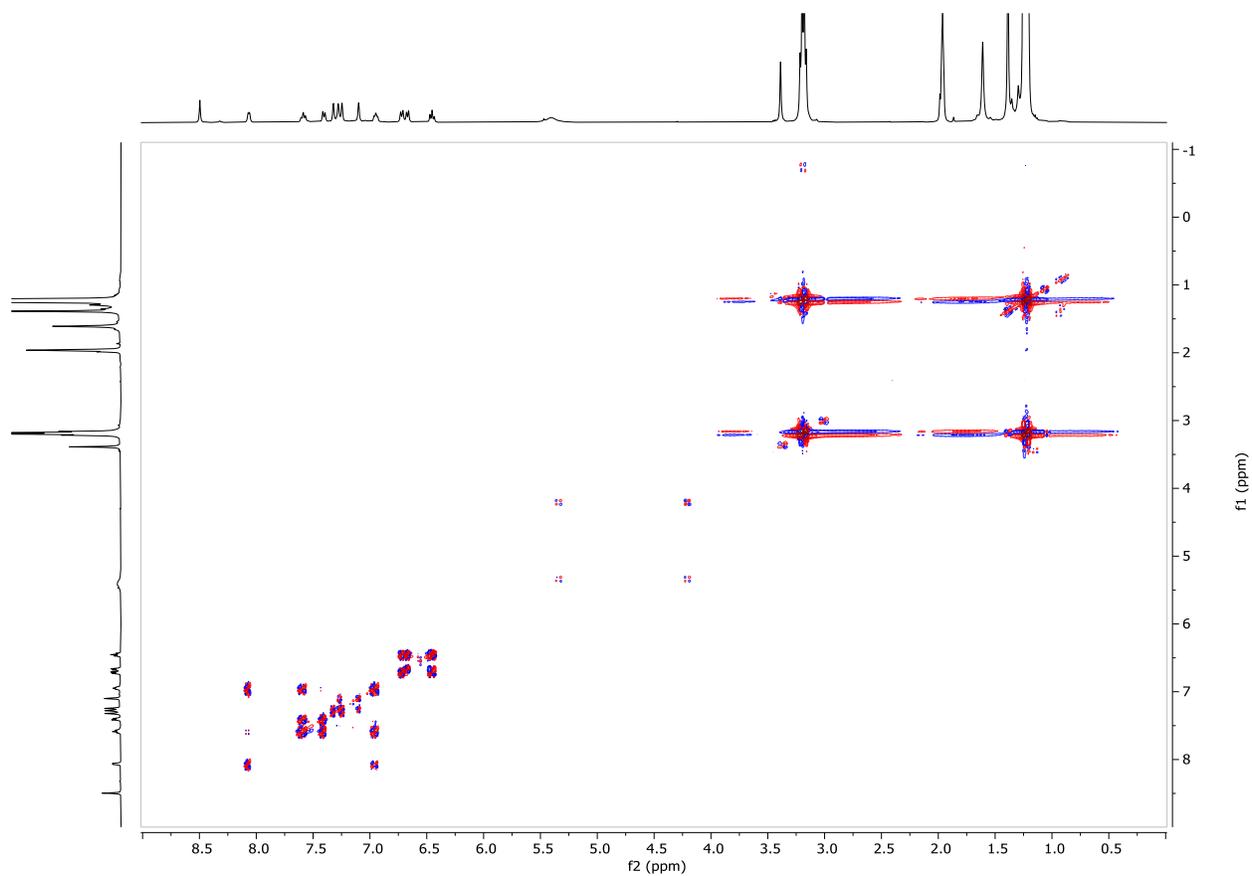
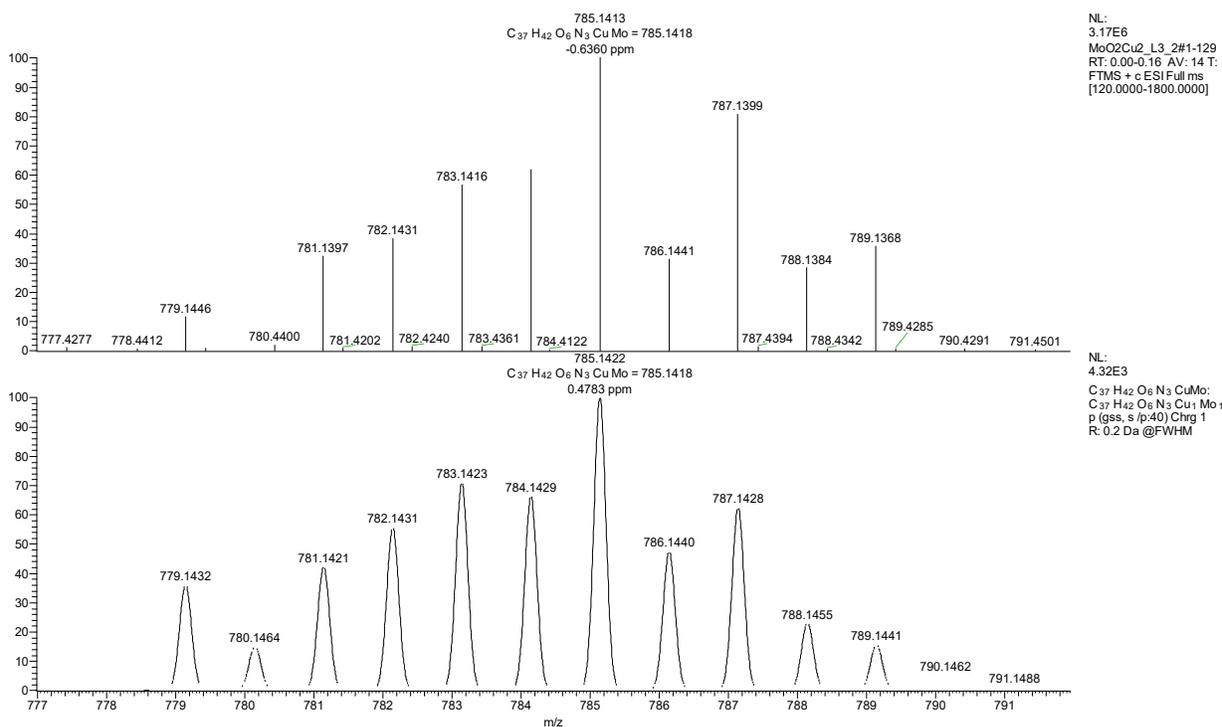**Figure S8.** ^{1}H-^{1}H COSY NMR spectrum of (NEt$_4$)$_2$[{MoO$_3$(L^{cat})Cu}$_2$] (**2**) (CD$_3$CN, 400 MHz).

Figure S9. High-resolution mass spectrum of $(NEt_4)_2[\{MoO_3(L^{cat})Cu\}_2]$ (**2**) (top), demonstrating the peak attributed to $\{MoO_3(L^{cat})Cu\}^+$ (bottom).

5. Synthesis and Characterization of [MoO$_2$(L^{cat})$_2$Cu$_2$] (3)

Method A.

A 3 mL solution of L^{cat}H$_2$ (20 mg, 0.035 mmol, 1.0 equiv) in THF and a 3 mL solution of (NEt$_4$)$_2$[MoO$_4$] (15 mg, 0.035 mmol, 1.0 equiv.) in CH$_3$CN were prepared and cooled to -33 °C. The solution of cold L^{cat}H$_2$ was then added dropwise to a stirring solution of cold (NEt$_4$)$_2$[MoO$_4$]. The reaction mixture was stirred for 15 minutes, and 3 mL solution of tetrakis(acetonitrile)copper(I) hexafluorophosphate [Cu(NCMe)$_4$](PF$_6$) (13 mg, 0.035 mmol, 1.0 equiv.) was added. The reaction mixture was stirred for 5 minutes, after which the volatiles were removed in vacuo to yield a dark orange solid (28.5 mg, 0.0156 mmol, 90%). The crude product was then dissolved in CD$_3$CN and left at room temperature, leading to the formation of orange precipitate. After 24 h, the solution was decanted, the resulting precipitate was dried for 2 h in vacuo, and recrystallized from DCM/ether to give 20 mg of **3** as yellow crystals (0.011 mmol, 63%). The yield was calculated based on the chemical formula obtained from the crystal structure of **3** that includes co-crystallized solvents (see Table S1). The residual CH$_3$CN solution (after the separation of precipitated **3**) was subjected to HRMS, which indicated the presence of (NEt$_4$)$_2$[MoO$_4$].

Method B.

A 3 mL solution of L^{cat}H$_2$ (20 mg, 0.035 mmol, 2.0 equiv) in THF and a 3 mL solution of (NEt$_4$)$_2$[MoO$_4$] (7.3 mg, 0.017 mmol, 1.0 equiv) in CH$_3$CN were prepared and cooled to -33 °C. The solution of cold L^{cat}H$_2$ was then added dropwise to a stirring solution of cold (NEt$_4$)$_2$[MoO$_4$]. The reaction mixture was stirred for 15 minutes and 3 ml solution of tetrakis(acetonitrile)copper(I) hexafluorophosphate [Cu(NCMe)$_4$](PF$_6$) (13.0 mg, 0.035 mmol, 2.0 equiv) was added. The reaction mixture was stirred for 5 minutes, after which the volatiles were removed in vacuo to produce a orange solid and crude product was recrystallized using DCM/ether to give 21 mg of **3** obtained as yellow crystals of **3** (0.012 mmol, 71%). The yield was calculated based on the chemical formula obtained from the crystal structure of **3** that includes co-crystallized solvents (see Table S1).
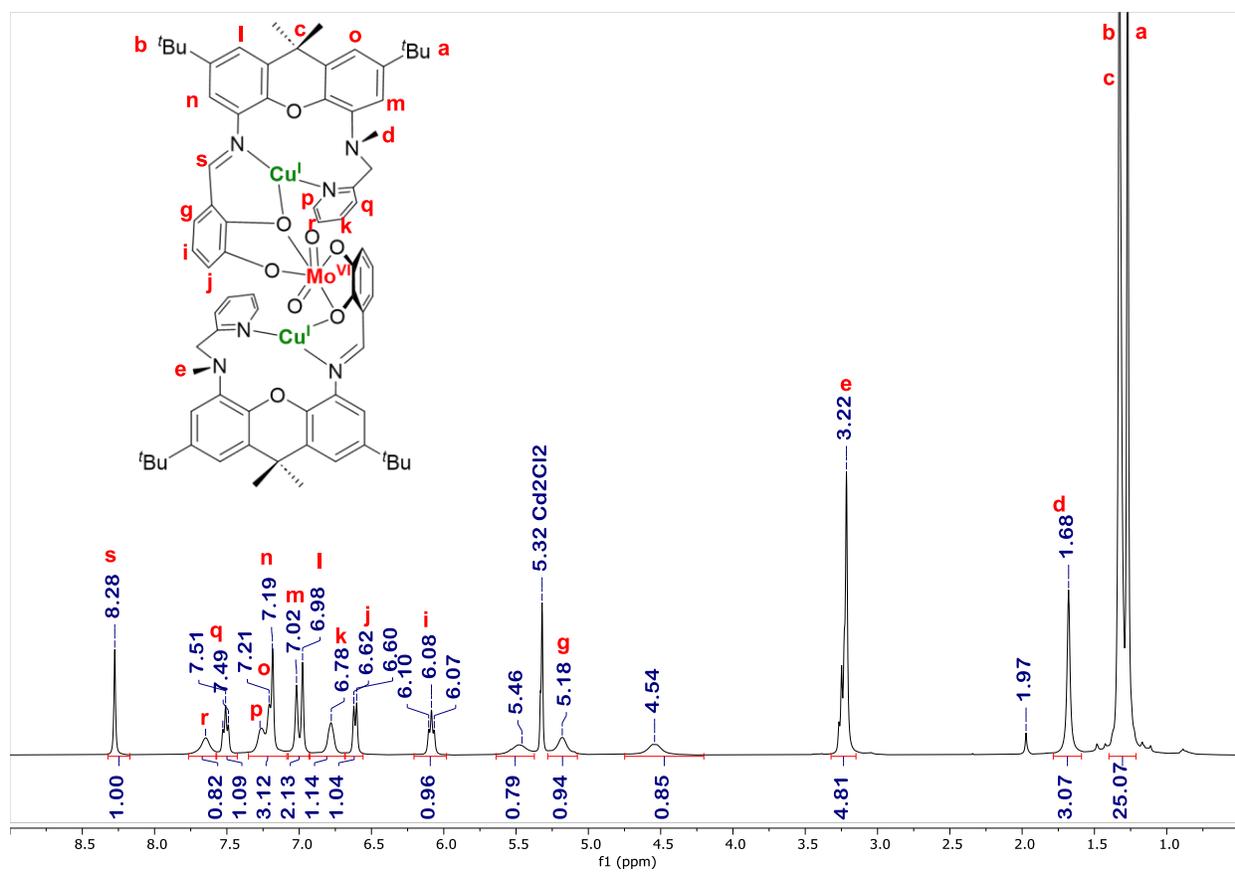
Figure S10. ^{1}H NMR (400 MHz, CD$_3$CN) of the reaction of L^{cat}H$_2$ (2 equiv) with (NEt$_4$)$_2$MoO$_4$ (1 equiv) and [Cu(NCMe)$_4$](PF$_6$) (2 equiv).
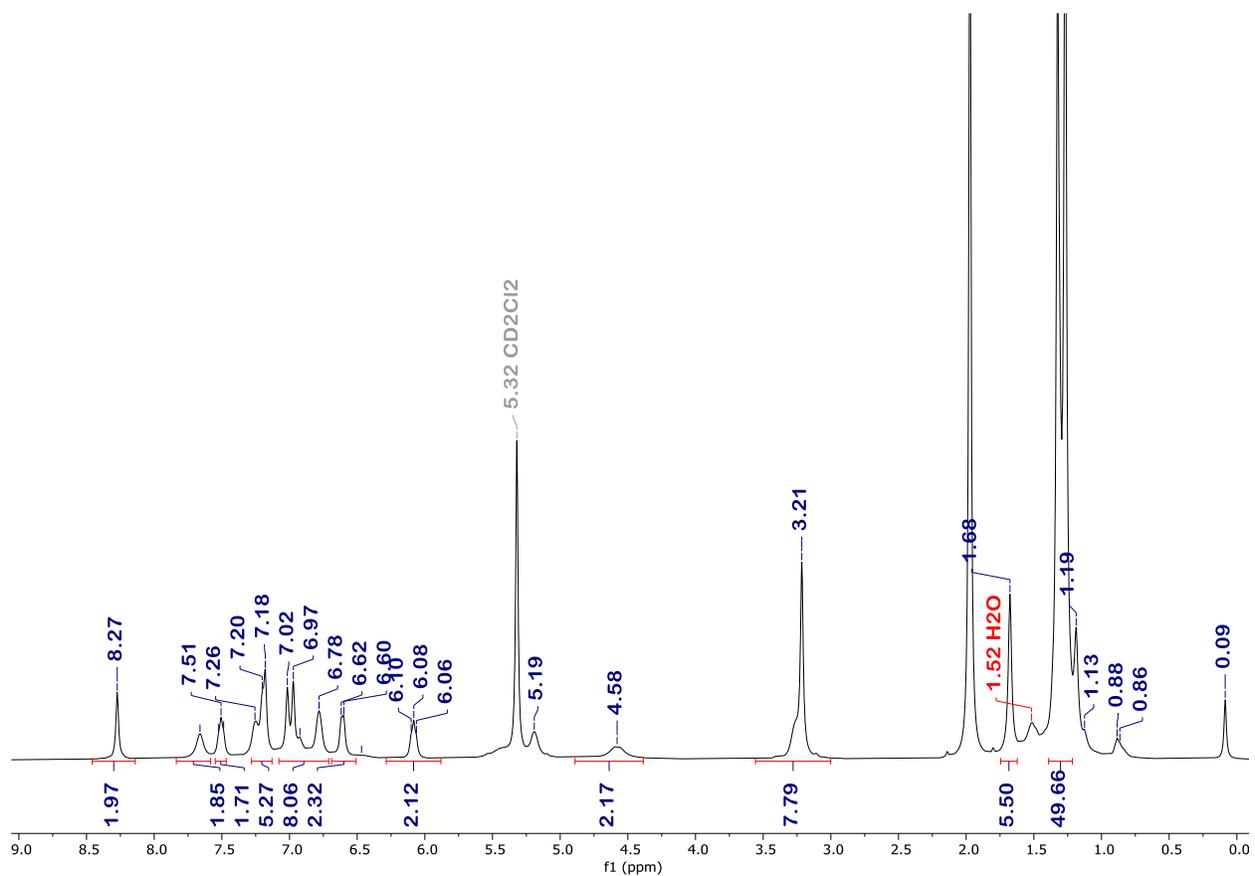
Figure S11. ^{1}H NMR (400 MHz, CD$_2$Cl$_2$) of the precipitate (complex **3**) formed in CD$_3$CN solution.
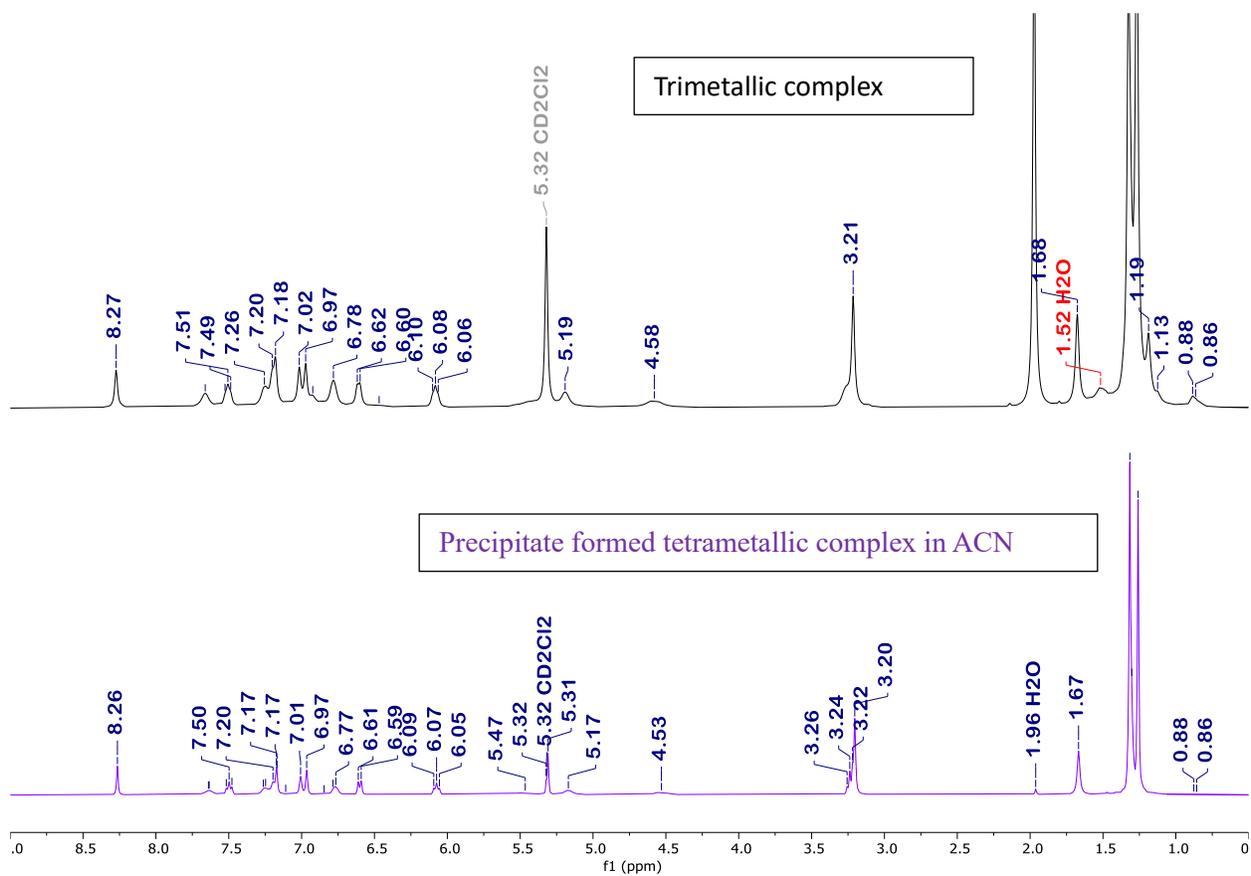
Figure S12. Comparison of ^1H NMR spectra of (bottom) **3** formed as a result of the decomposition of tetrametalic complex and (top) **3** obtained directly from $L^{cat}H_2$, $2[MoO_4]^{2-}$ and $2[Cu(NCMe)_4]^+$.
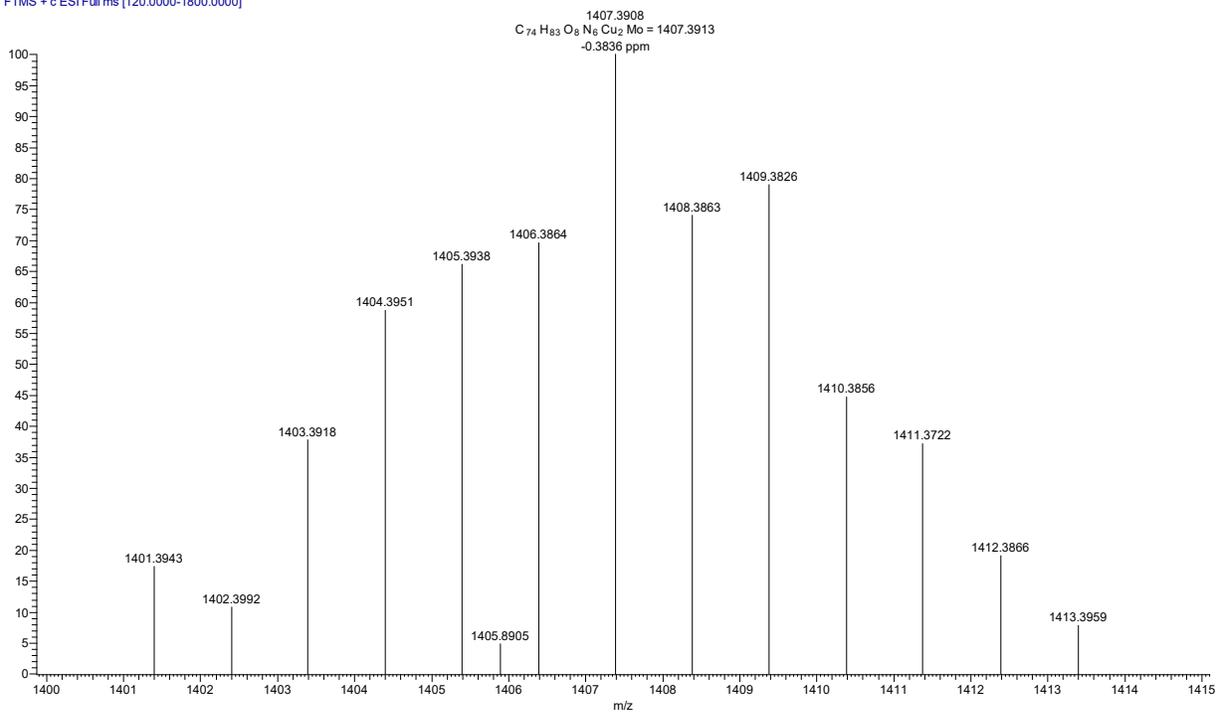
Figure S13. High-resolution mass spectrum of $(NEt_4)_2[MoO_2(L^{cat})_2Cu_2]$ (**3**), demonstrating the peak attributed to $[M+H]^+$
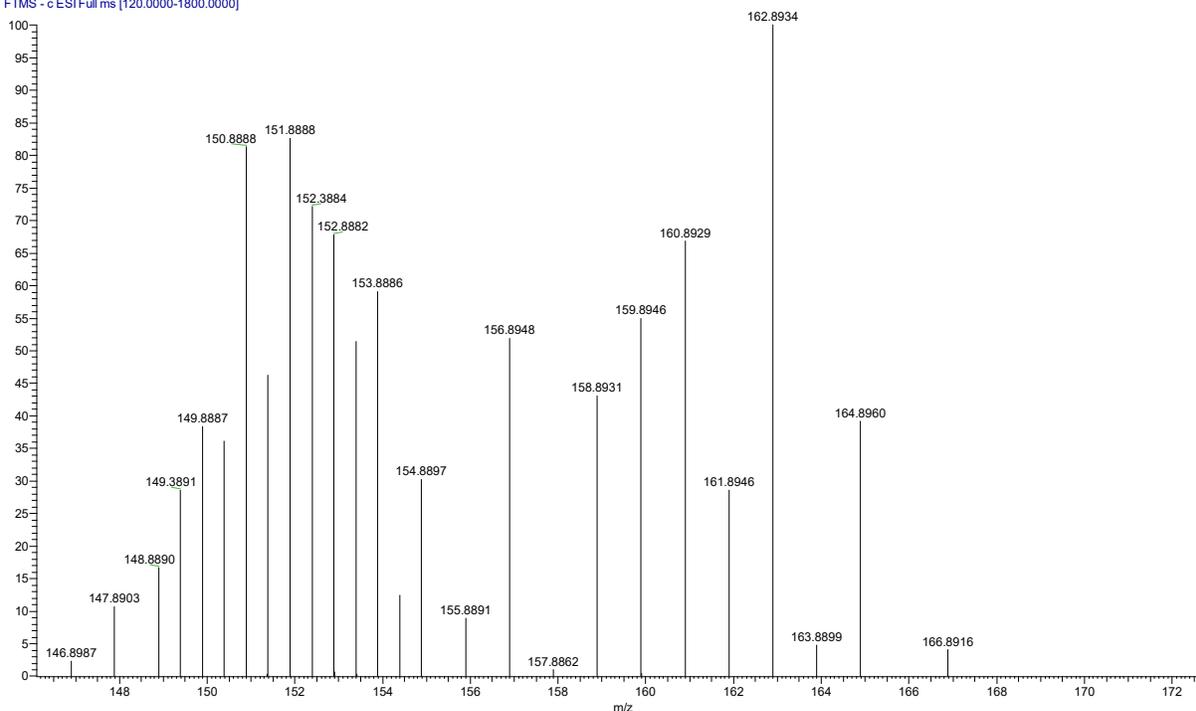
Figure S14. High-resolution mass spectrum of the residual solution from the decomposition of **2** (after the crystallization of **3**), demonstrating the peak attributed to molybdate (m/z of $[MoO_4H]^+$ = 162.8929). The peak on the left is likely indicative of $[Mo_2O_7]^{2-}$.

6. Kinetic Experiment: Monitoring of the Decomposition of Tetrametallic complex $(NEt_4)_2[\{MoO_3(L^{cat})Cu\}_2]$ via ^1H NMR spectroscopy

The kinetics of the decomposition of the tetrametallic complex $(NEt_4)_2[\{MoO_3(L^{cat})Cu\}_2]$ (2) in CD_3CN were monitored by time-resolved ^1H NMR spectroscopy in solution.

Sample Preparation

The tetrametallic complex $(NEt_4)_2[\{MoO_3(L^{cat})Cu\}_2]$ (2) was prepared as per the preparation procedure above. The product (0.025 mmol) was dissolved in 0.6 mL of CD_3CN. Mesitylene (0.018 mmol) was used as an internal standard. The solution was transferred into a J. Young NMR tube, sealed, and mixed thoroughly.

NMR Data Acquisition

^1H NMR spectra were recorded on a 400 MHz spectrometer at 298 K. An initial spectrum was acquired immediately after sample preparation (t = 0). Subsequent spectra were collected at defined time intervals (e.g., every 1 hour) over a total period of up to 22 hours. The spectrometer acquisition parameters were held constant throughout the experiment to ensure consistent integration, with the following settings used: spectral width = 8012.8 Hz, acquisition time = 4.09 s, relaxation delay = 2.0 s, and number of scans = 32.

Data Analysis

Distinct non-overlapping signals corresponding to the tetrametallic starting material were identified and assigned based on chemical shift, integration, and prior characterization. The integrals of selected signals were normalized relative to the internal standard to account for any volume loss or fluctuation. Plots of concentration vs. time were constructed using integrated signal intensities, and kinetic parameters (e.g., rate constant and reaction order) were extracted by fitting the data to standard kinetic models (zeroth order, first order, and second order).

To confirm the reaction order, a plot of $\ln((NEt_4)_2[\{MoO_3(L^{cat})Cu\}_2])$ vs. time (according to $\ln[A] = -kt + \ln[A]_0$) was used to assess first-order behavior. Rate constants were obtained from the slope of the best-fit line with R^2 near 1.

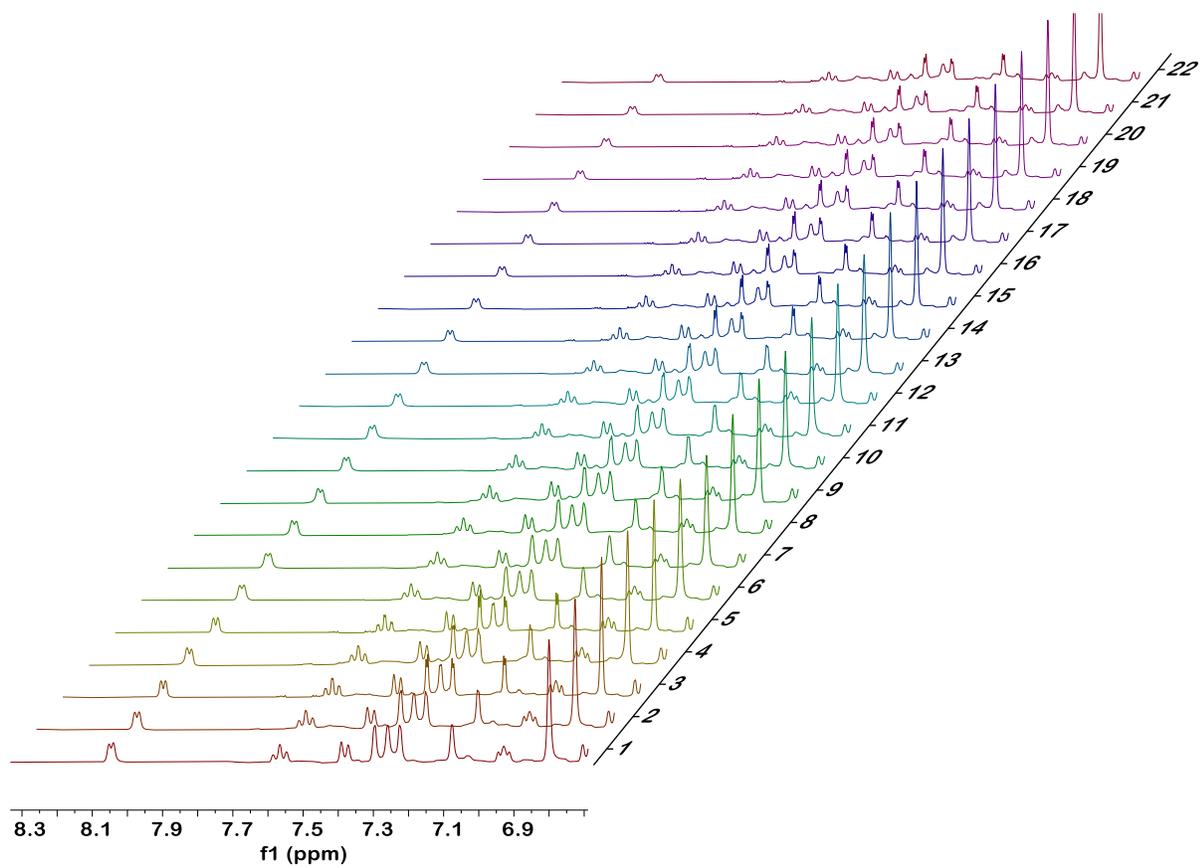**Figure S15.** ^{1}H NMR (aromatic region) of the decomposition of tetrametallic complex into trimetallic complex over the 22 hours.

The decomposition of tetrameticllic complex into trimetallic complex

y = -8E-06x - 5.2178
R² = 0.9927

ln[Concentration]

Time/s
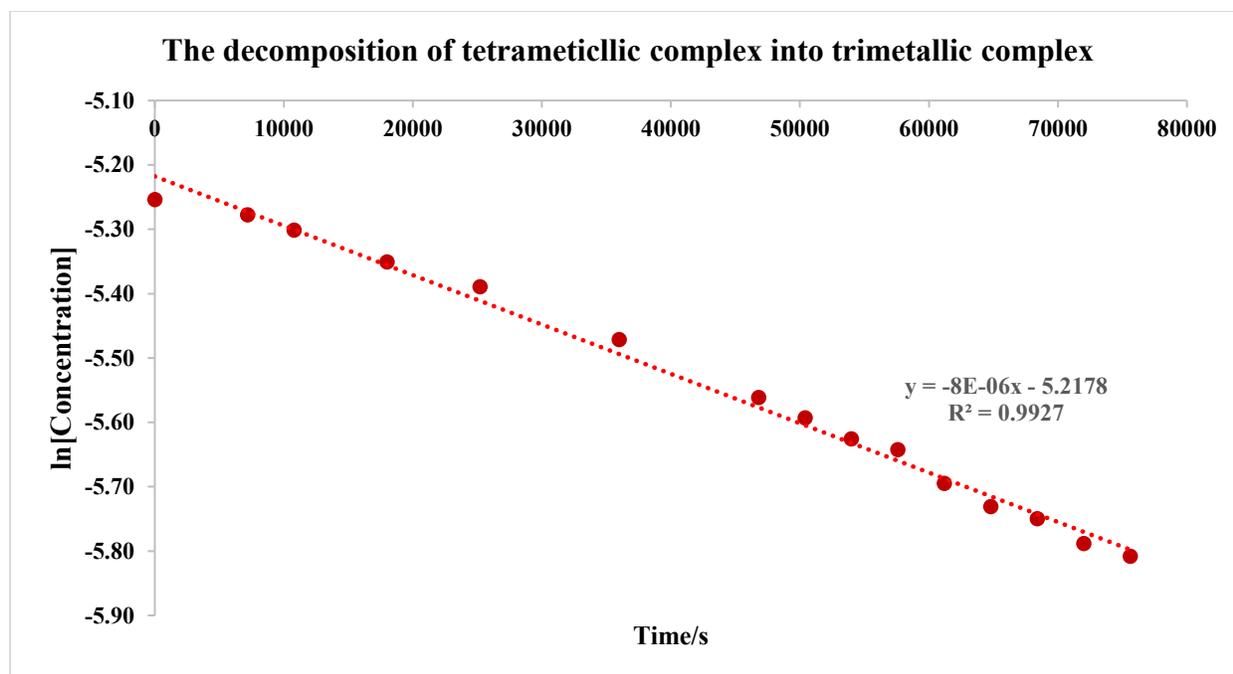
Figure S16. Rate of decomposition of $(NEt_4)_2[\{MoO_3(L^{cat})Cu\}_2]$ (**2**): first order with k = 8.0 X 10^{-6} s^{-1}.

7. X-ray crystallographic details

The structures of complexes **2** and **3** were determined by X-ray crystallography. Suitable crystals were collected on a Bruker D8 Venture diffractometer with kappa geometry, an Incoatec IµS micro-focus source X-ray tube (CuK$_\alpha$ and MoK$_\alpha$ radiation, respectively), a multilayer mirror for monochromatization, and a Photon III CPAD area detector. The data were processed using APEX software (SAINT and SADABS for integration and scaling, respectively). The structures were solved and refined using SHELXT[4] and difference Fourier (ΔF) maps, as embedded in SHELXL-2019/3[5] running under Olex2.[6] The hydrogen atoms were placed in calculated positions using a standard riding model and refined isotropically; all other atoms were refined anisotropically. Additionally, both crystal structures exhibited disorder with the ligands, especially the t-butyl groups, as well as significant solvent disorder. Complex **3** used a Solvent Mask to remove three diethyl ether solvent molecules that were unstable to model. The experimental crystallographic parameters are reported in Table S1.

Table S1. Experimental crystallographic parameters for **2** and **3**.

Complex	2	3
Formula	$C_{74}H_{82}Cu_2Mo_2N_6O_{12}*2(C_8H_{20}N)*5$ $.658(C_2H_{2.999}N)*1.16(H_2O)$	$C_{74}H_{79.464}Cu_2MoN_6O_8*0.5(CH_2Cl_2)$ $*4.5(C_4H_{10}O)$
Fw, g/mol	2079.97	1779.92
Temperature, K	100	100
Crystal System	monoclinic	triclinic
Space Group	$P2_1/c$	P-1
Color	dark orange	colorless
Z	2	2
a, Å	20.6595(12)	14.5885(10)
b, Å	17.8045(10)	18.5886(12)
c, Å	14.3818(8)	18.8023(13)
α, deg	90.00	66.937(2)
β, deg	96.268(3)	81.633(2)
γ, deg	90.00	84.113(2)
V, Å^3	5258.5(5)	4635.5(5)
d_{calcd}, g/cm^3	1.314	1.275
μ, mm^{-1}	2.879	0.678
$R_1{}^a$ (all data)	0.1166	0.1437
$wR_2{}^b$ (all data)	0.1876	0.3020
$R_1{}^a$ [(I>2σ)]	0.0732	0.0903
$wR_2{}^b$ [(I>2σ)]	0.1641	0.2592
GOF (F^2)	1.015	1.012

[a] $R_1 = \sum||F_o - |F_c||/\sum|F_o|$. [b] $wR_2 = (\sum (w(F_o{}^2 - F_c{}^2)^2)/\sum(w(F_o{}^2)^2))^{1/2}$. [c] $GOF = (\sum w(F_o{}^2 - F_c{}^2)^2/(n - p))^{1/2}$ where n is the number of data and p is the number of parameters refined.

8. Computational Details

Geometry optimizations were performed at the BP86/def2-SVP/SMD(MeCN) level of theory as implemented in ORCA 6.1.0 using default numerical settings.[7] All optimized structures were confirmed to be minima based on analysis of the harmonic frequencies, and standard thermodynamic approximations were used to estimate the Gibbs free energy.[8] The tetrametallic species were all optimized as dianions based on the experimental formula $(NEt_4)_2[\{MoO_3Cu(L^{cat})\}_2]$. The methyl and ^tBu groups on the xanthene backbone of L^{cat} were replaced by H to save on computational time (though the most important species **2** and **3** were also optimized with the full ligand structure, see below). Upon loss of molybdate, the resulting trimetallic structure $[MoO_2\{CuL^{cat}\}_2]$ was optimized as a neutral species. Every compound was optimized as a closed-shell singlet. Single point energy refinements were performed at the BP86-D4/def2-TZVP/SMD(MeCN), B3LYP-D4/def2-TZVP/SMD(MeCN), and ω-B97X-D4/def2-TZVP/SMD(MeCN) levels of theory.[7,9] Refined free energies were calculated using **Eq. S1**. B3LYP free energies are reported in the manuscript; results differed quantitatively but not qualitatively between the three functionals, as shown in **Table S2**. Full thermodynamics for each optimized species are located in **Table S3**.

$$G_{TZ} = G_{DZ} - E_{DZ} + E_{TZ} \tag{S1}$$

The crystallographic structure of $(NEt_4)_2[\{MoO_3Cu(L^{cat})\}_2]$ was used for the initial computational geometry removing tetraethylammonium cations, solvent molecules, and making the ligand simplifications described above to generate **2**. For non symmetric structures we performed linear optimizations by elongating the Mo-Mo distance and all Mo-O distances in the diamond core (to one side of the symmetric molecule) to generate intermediates **i-iii** discussed in the paper and a higher energy (+31.70 kcal/mol) intermediate **vi**. The Mo-Mo elongation only resulted in the dimer fragmenting into symmetric monomers. Larger pictures (than **Fig. 4** of the Communication) of **2**, **i-iii**, and **vi** are shown in **Figs. S17-S21**. Deleting molybdate from **2** or these non-symmetric structures optimized to one of **3**, **iv**, or **v**. Once again, larger pictures of **3**, **iv**, and **v** are shown in **Figs. S22-S24**. Along these scans the highest energy structures were used to attempt to optimize transition states connecting these intermediates unsuccessfully. Nudged elastic band calculations[10-12] between the most promising intermediates suggested we were not missing additional intermediates, but did not result in successful transition state optimizations.

To test the appropriateness of the ligand simplifications, we fully optimized intermediates 2_{full} and 3_{full} as shown in **Fig. S25** and **Fig. S26**. Recall that the small model reaction free energy for $2 \rightarrow 3 + [MoO_4]^{2-}$ was +11.62 kcal/mol; this compares well to the full model reaction energy for $2_{full} \rightarrow 3_{full} + [MoO_4]^{2-}$ that was +12.61 kcal/mol. **Table S2** shows the relative free energies of all intermediates computed with all three functionals. **Table S3** shows all of the components used to compute the absolute free energies used to derive those relative free energies. Finally, cartesian coordinates for all optimized structures may be found in the ESI xyz file.
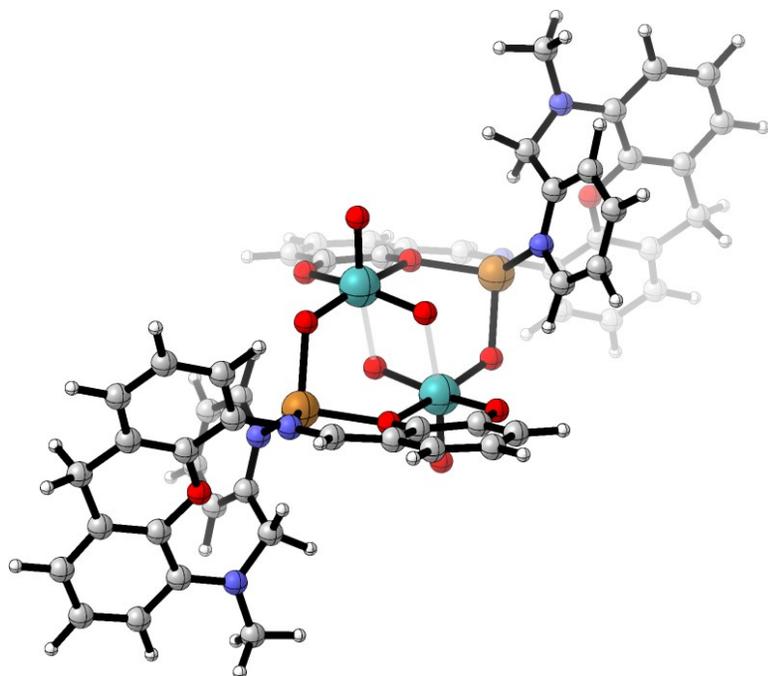
Fig. S17. Optimized structure of **2**.
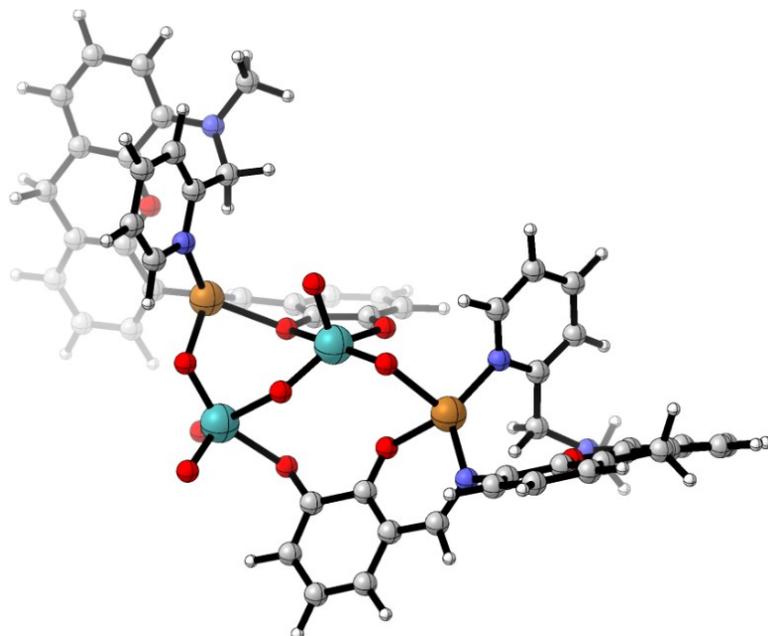
Fig. S18. Optimized structure of **i**.
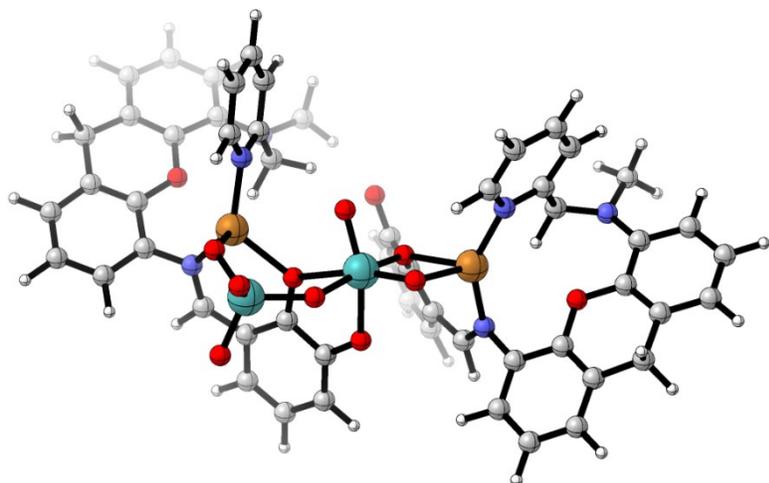
Fig. S19. Optimized structure of **ii**.

Fig. S20. Optimized structure of **iii**.

Fig. S21. Optimized structure of **vi**.

Fig. S22. Optimized structure of **3**.

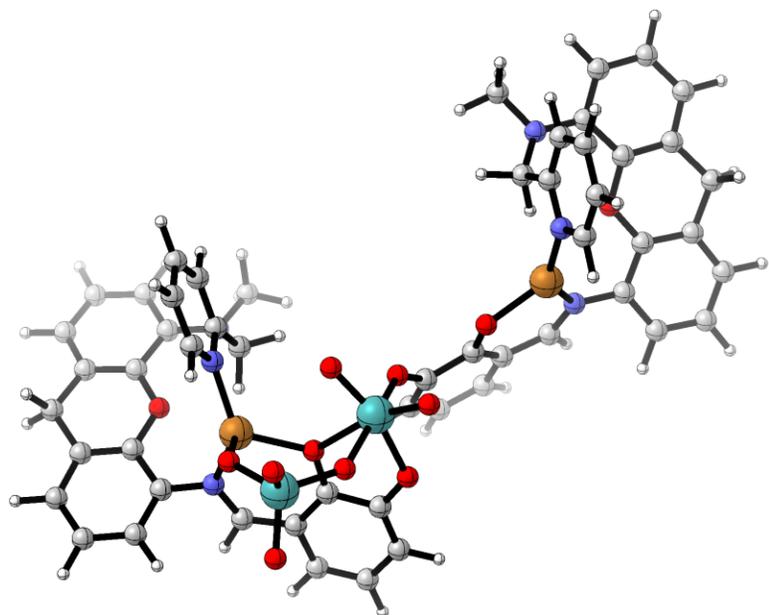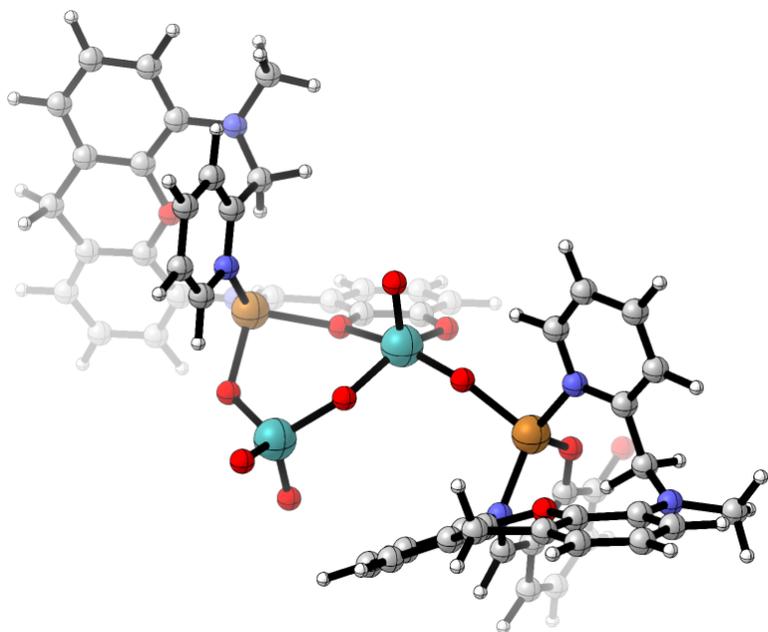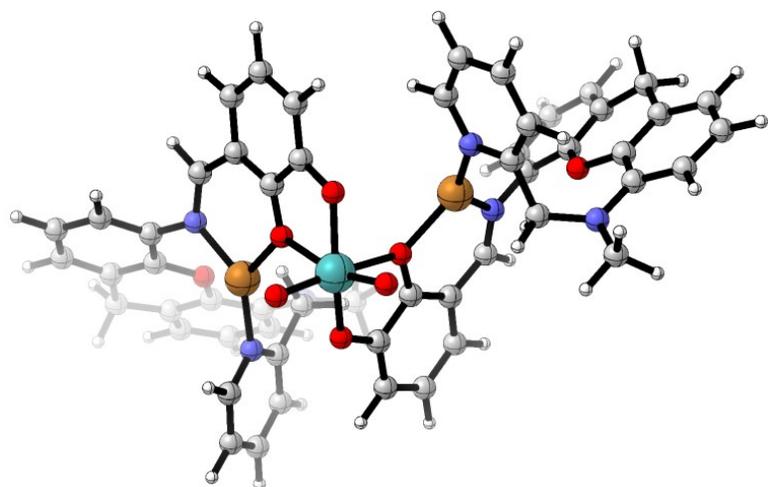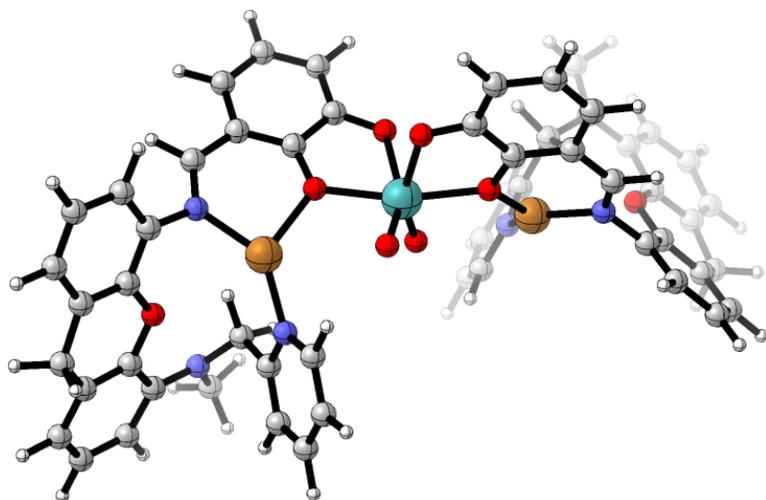**Fig. S23.** Optimized structure of **iv**.
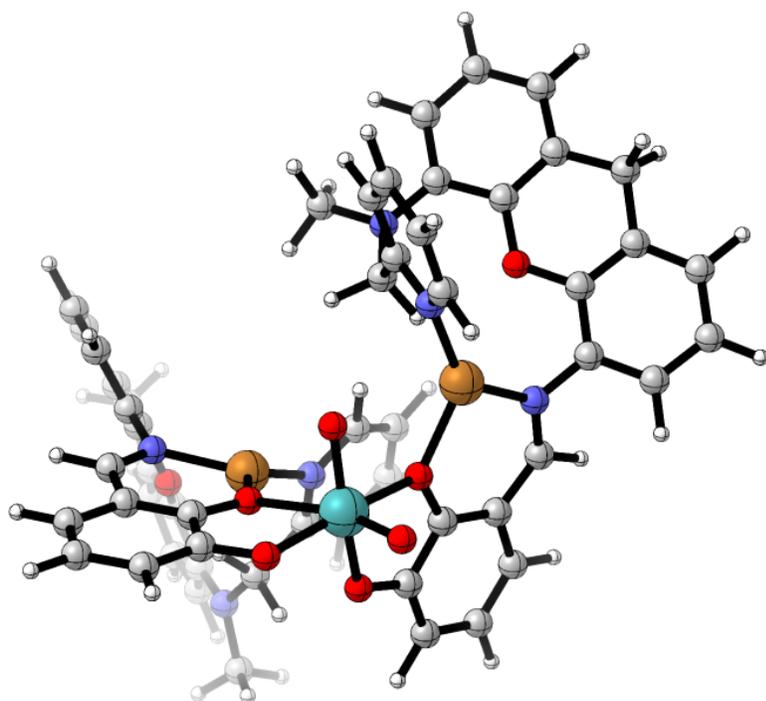
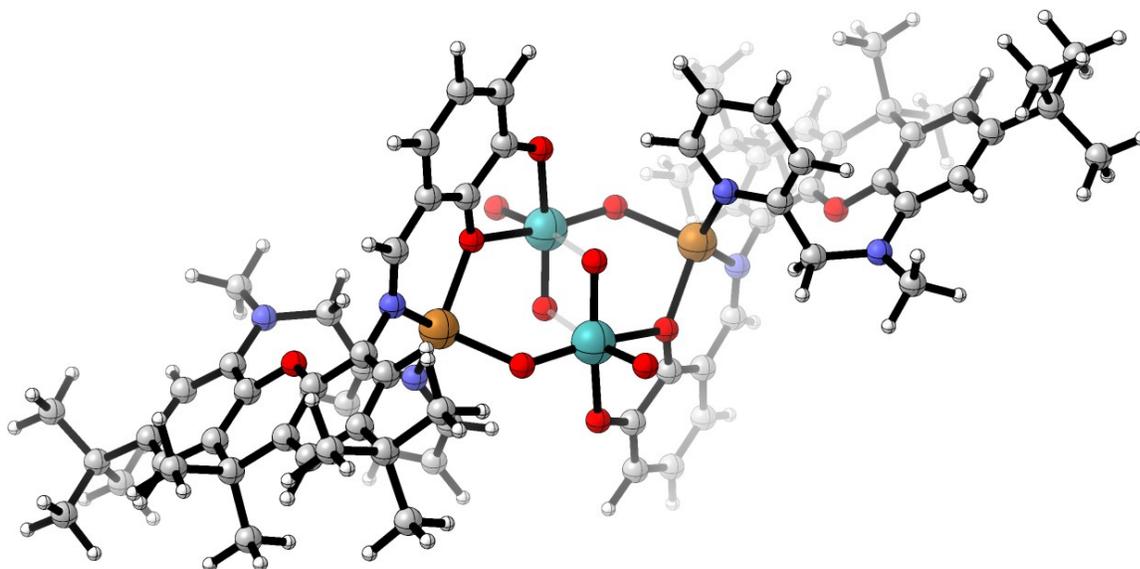**Fig. S24.** Optimized structure of **v**.

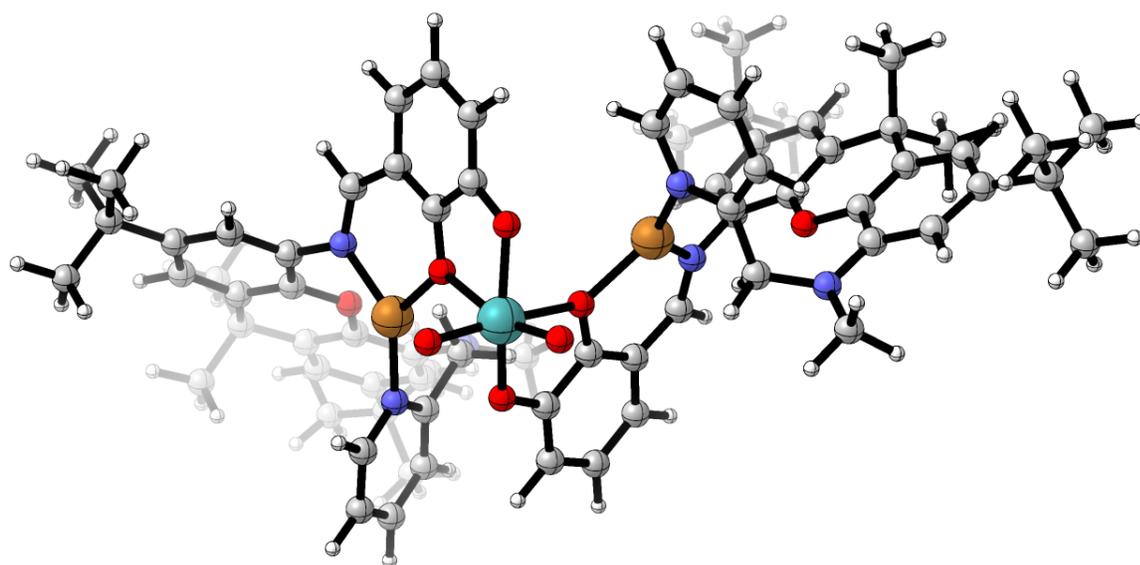**Fig. S25.** Optimized structure of **2_full**.

Fig. S26. Optimized structure of **3_full**.

Table S2. Relative free energies (in kcal/mol) of intermediates calculated with BP86-D4/def2-TZVP/SMD(MeCN), B3LYP-D4/def2-TZVP/SMD(MeCN), and ω-B97X-D4/def2-TZVP/SMD(MeCN).

Species	BP86	B3LYP	ω-B97X
2	0.00	0.00	0.00
i	23.41	23.42	27.00
ii	20.16	20.88	28.09
iii	15.62	13.52	18.95
vi	31.33	31.70	40.02
3	17.13	11.62	16.78
iv	32.18	25.19	29.06
v	21.67	16.65	22.75
2$_{full}$	0.00	0.00	0.00
3$_{full}$	18.13	12.61	17.15

Table S3. Thermodynamics (in E_h) for all fully optimized species. BP = BP86, B3 = B3LYP, wB = ω-B97X, DZ = def2-SVP, and TZ = def2-TZVP.

Species	Charge	$E_{BP/DZ}$	$G_{BP/DZ}$	$E_{BP/TZ}$	$E_{B3/TZ}$	$E_{wB/TZ}$
2	2-	-6730.579478	-6729.825265	-6735.037724	-6734.327970	-6735.071773
i	2-	-6730.541087	-6729.789123	-6734.998171	-6734.288388	-6735.026495
ii	2-	-6730.541868	-6729.789125	-6735.004129	-6734.293223	-6735.025536
iii	2-	-6730.555360	-6729.805509	-6735.008475	-6734.302057	-6735.037215
vi	2-	-6730.527277	-6729.775932	-6734.984922	-6734.274584	-6735.005133
3	0	-6361.083227	-6360.336386	-6365.135021	-6364.557550	-6365.292795
[MoO$_4$]$^{2-}$	2-	-369.430763	-369.449282	-369.849508	-369.726016	-369.726342
iv	0	-6361.074611	-6360.327897	-6365.110915	-6364.535788	-6365.273110
v	0	-6361.077997	-6360.330518	-6365.128428	-6364.550171	-6365.283915
2$_{full}$	2-	-7516.232806	-7514.965970	-7521.651641	-7520.999238	-7522.137118
3$_{full}$	0	-7146.737231	-7145.476369	-7151.748743	-7151.228631	-7152.358944

Figure S27. Geometry optimized structures with relative free energies (kcal/mol) for the benzenedithiolate analogues of our ligand.

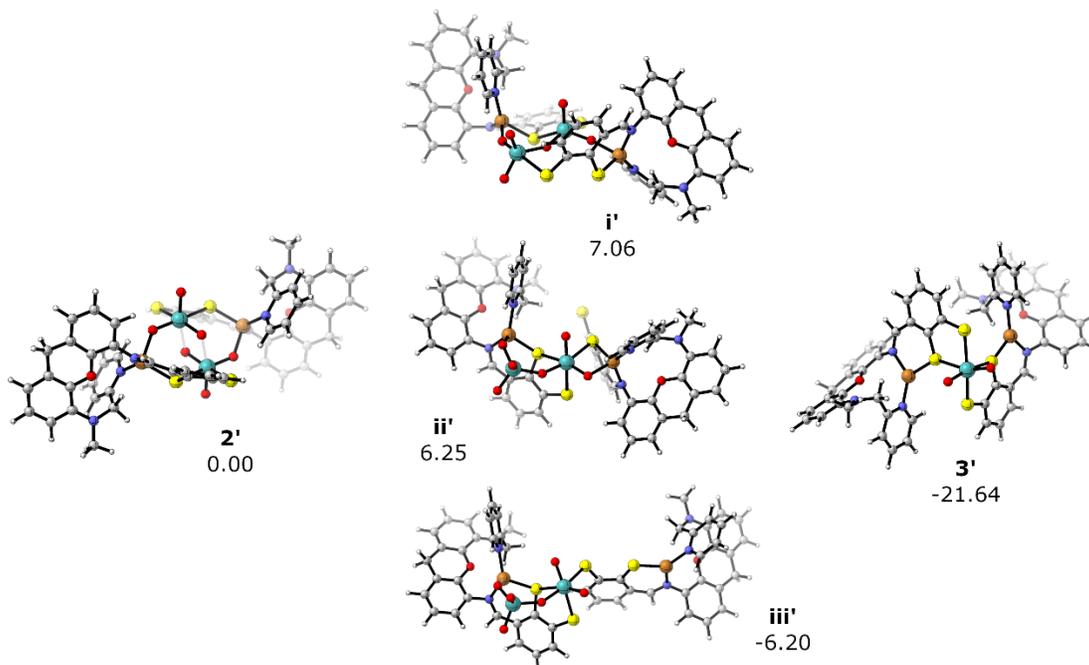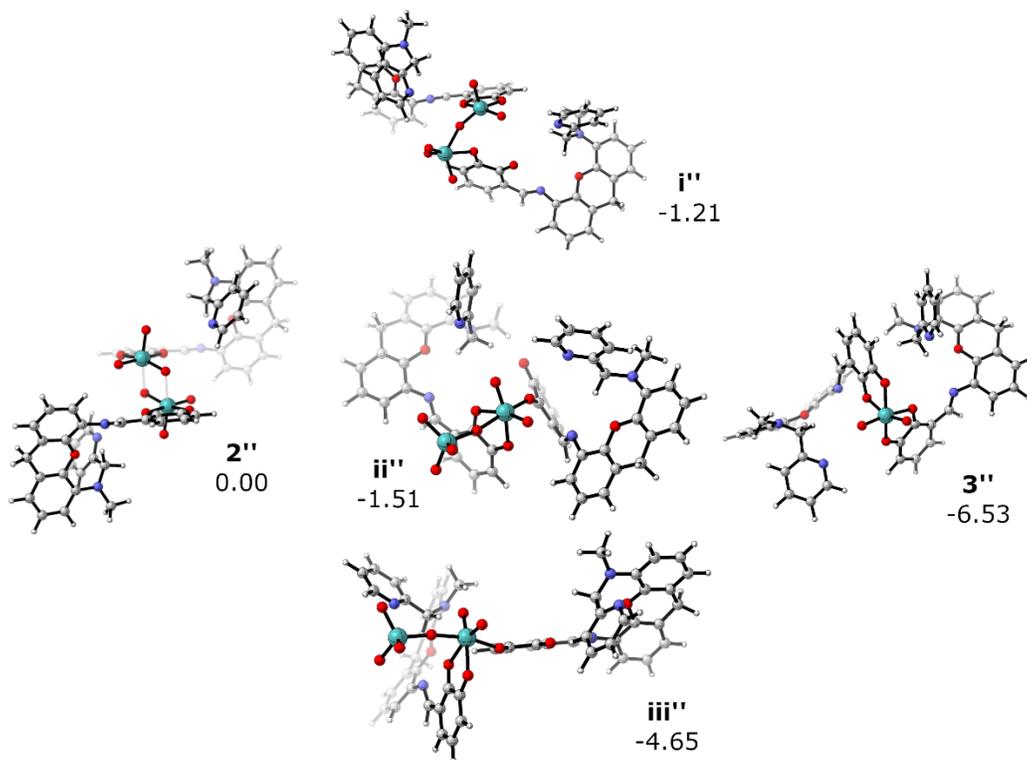i'
7.06

2'
0.00

ii'
6.25

3'
-21.64

iii'
-6.20

Figure S28. Geometry optimized structures with relative free energies (kcal/mol) for analogues of our complexes without the Cu(I) ions.

i''
-1.21

2''
0.00

ii''
-1.51

3''
-6.53

iii''
-4.65

Because the enzymatic system contains MPT as bidentate ligands to Mo(VI), we computationally substituted benzenedithiolate for catecholate in our ligand (**Figure Sx**) to see how that would alter the structures and thermodynamics of the intermediates presented in **Fig. 4** of the manuscript. Structurally, intermediates **2'**, **i'**, **ii'**, **iii'**, and **3'** are quite similar to their catecholate analogues with a few subtle differences: (i) the diamond core of **2'** features more out of plane bending of benzenedithiolate presumably due to the larger S atoms and (ii) the benzenedithiolate bridging Mo(VI) and Cu(I) in **i'** has reoriented up vs. down in **i**. Thermodynamically, we observe **iii'** to be favored amongst the rearranged tetrametallic intermediates similar to our system, however, this rearrangement is now exergonic by 6.2 kcal/mol as compared to catecholate where it is endergonic by 13.5 kcal/mol. This suggests that if the tetrametallic intermediate we observed forms for this related ligand system, rearrangement to position molybdate for loss should be more accessible. Moreover, loss of molybdate to form **3'** is exergonic by 21.6 kcal/mol.

Cu(I) is not present in the active site of many enzymes featuring bis(MPT) ligated Mo/W. Therefore, we also evaluated the thermodynamics of the rearrangement of our system removing the two Cu(I) ions for important intermediates from **Fig. 4** of the manuscript (**Figure Sy**). The more open bimetallic structures of **i''**, **ii''**, and **iii''** are slightly favored over **2''**, presumably due to electrostatic relief in these now tetraanionic species. Loss of molybdate to form dianionic **3''** is exergonic by 6.53 kcal/mol.

Table S4. Thermodynamics (in E_h) for all fully optimized species. BP = BP86, B3 = B3LYP, wB = ω-B97X, DZ = def2-SVP, and TZ = def2-TZVP.

Species	Charge	$E_{BP/DZ}$	$G_{BP/DZ}$	$E_{BP/TZ}$	$E_{B3/TZ}$	$E_{wB/TZ}$
2	2-	-6730.579478	-6729.825265	-6735.037724	-6734.327970	-6735.071773
i	2-	-6730.541087	-6729.789123	-6734.998171	-6734.288388	-6735.026495
ii	2-	-6730.541868	-6729.789125	-6735.004129	-6734.293223	-6735.025536
iii	2-	-6730.555360	-6729.805509	-6735.008475	-6734.302057	-6735.037215
vi	2-	-6730.527277	-6729.775932	-6734.984922	-6734.274584	-6735.005133
3	0	-6361.083227	-6360.336386	-6365.135021	-6364.557550	-6365.292795
[MoO₄]²⁻	2-	-369.430763	-369.449282	-369.849508	-369.726016	-369.726342
iv	0	-6361.074611	-6360.327897	-6365.110915	-6364.535788	-6365.273110
v	0	-6361.077997	-6360.330518	-6365.128428	-6364.550171	-6365.283915
2_full	2-	-7516.232806	-7514.965970	-7521.651641	-7520.999238	-7522.137118
3_full	0	-7146.737231	-7145.476369	-7151.748743	-7151.228631	-7152.358944
2'	2-	-8022.321553	-8021.578683	-8026.640332	-8025.780546	-8026.384695
i'	2-	-8022.295031	-8021.555700	-8026.621672	-8025.765754	-8026.365129
ii'	2-	-8022.302738	-8021.561720	-8026.626948	-8025.768737	-8026.369854
iii'	2-	-8022.309008	-8021.569704	-8026.641352	-8025.786861	-8026.388681
3'	0	-7652.837657	-7652.102763	-7656.787940	-7656.062522	-7656.670206
2''	4-	-3449.509225	-3448.759433	-3452.868417	-3452.554353	-3453.371235
i''	4-	-3449.488920	-3448.742032	-3452.857289	-3452.553385	-3453.389643
ii''	4-	-3449.492868	-3448.745629	-3452.857112	-3452.554213	-3453.374281
iii''	4-	-3449.512675	-3448.762944	-3452.867616	-3452.561705	-3453.383105
3''	2-	-3080.073217	-3079.325908	-3083.005685	-3082.817741	-3083.629881

9. References

1. Bheemaraju, A.; Beattie, J. W.; Danylyuk; Y.; Rochford, J.; Groysman, S. Synthesis, Structures, and Reactivity of Copper(I) Complexes Supported by a Rigid Dinucleating Ligand. *Eur. J. Inorg. Chem.* **2014**, *34*, 5865-5873.

2. Cotton, F. A.; Donahue, J. P.; Murillo, C. A. Quadridentate Bridging EO_4^{2-} (E = S, Mo, W) Ligands and Their Role as Electronic Bridges. *Inorg. Chem.* **2001**, *40*, 2229-2233.

3. Kaluarachchige Don, U. I. Synthesis and Reactivity of Xanthene-Based Heterobimetallic Systems for CO Oxidation. Ph.D. Dissertation, Wayne State University, Detroit, MI, 2024. https://www.proquest.com/openview/8ff71bf1d06e0ab67b0036fd97dfb0ce/

4. Sheldrick, G., SHELXT - Integrated space-group and crystal-structure determination. *Acta Cryst. Section A* **2015**, *71*, 3-8.

5. Sheldrick, G., Crystal structure refinement with SHELXL. *Acta Cryst. Section C* **2015,** *71*, 3-8.

6. Dolomanov, O. V.; Bourhis, L. J.; Gildea, R. J.; Howard, J. A. K.; Puschmann, H., OLEX2: a complete structure solution, refinement and analysis program. *J. Appl. Crystallogr.* **2009**, *42*, 339-341.

7. Most methods and the software were already cited in the Communication; see References 25-40.

8. Schlegel, H. B. Geometry optimization. *WIREs Comput. Mol. Sci.* **2011**, *1*, 790-809.

9. Chai, J.-D.; Head-Gordon, M. Long-range corrected hybrid density functionals with damped atom-atom dispersion corrections. *Phys. Chem. Chem. Phys.* **2008**, *10*, 6615-6620.

10. Mills, G.; Jónsson, H.; Schenter, G. K. Reversible Work Transition State Theory: Application to Dissociative Adsorption of Hydrogen. *Surf. Sci.* **1995**, *324*, 305–337.

11. Henkelman, G.; Jónsson, H. Improved Tangent Estimate in the Nudged Elastic Band Method for Finding Minimum Energy Paths and Saddle Points. *J. Chem. Phys.*, **2000**, 113 (22), 9978–9985.

12. Ásgeirsson, V.; B.O., Birgirsson; Bjornsson, R.; Becker, U.; Riplinger, C.; Neese, F.; Jónssson, H. Nudged Elastic Band Method for Molecular Reactions Using Energy-Weighted Springs Combined with Eigenvector Following. *J. Chem. Theory Comput.*, **2021**, 17, 4929.